Granular Matter manuscript No.
(will be inserted by the editor)

N. Meejun · A.C. Skeldon · U. Tüzün · C. O'Sullivan

Wavelet analysis of DEM simulations of samples under biaxial compression

Received: date

Abstract The results of a wavelet analysis of data from discrete element modelling (DEM) simulations of samples under biaxial compression are presented. We show how a wavelet technique may be used to find the strain scales on which critical events occur and to identify regions both in space and in strain when particles in the sample undergo significant activity. The wavelet analysis indicates that most activity occurs along a line, and this line coincides with a localization or shear band that develops in the specimen during compression. The location of this shear band can be visually identified by considering the cumulative particle rotation. Furthermore, using cross-correlation we show that the principal stress ratio is correlated with the porosity of the sample along this line. In order to investigate the robustness of the technique, the wavelet analysis is carried out on two different size specimens that both show the same general phenomena.

Keywords Wavelet analysis · DEM simulation · biaxial compression

1 Introduction

Constructing a complete theoretical understanding of the behaviour of granular materials remains an open and challenging question. While significant insights have been gained through the use of continuum models, such

N. Meejun and U. Tüzün
Department of Chemical and Process Engineering, Faculty of Engineering and Physical Sciences, University of Surrey, GU2 7XH
Tel.: +44 1483 300800
Fax: +44 1483 259510
E-mail: n.meejun@surrey.ac.uk, u.tuzun@surrey.ac.uk

A.C. Skeldon
Department of Mathematics, Faculty of Engineering and Physical Sciences, University of Surrey, GU2 7XH
Tel.: +44 1483 682634
Fax: +44 1483 686071
E-mail: a.skeldon@surrey.ac.uk

C. O'Sullivan
Department of Civil and Environmental Engineering, Imperial College, London, SW7 2AZ
Tel.: +44
Fax: +44
E-mail: cath.osullivan@imperial.ac.uk

models have difficulty capturing the inhomogeneous behaviour that is characteristic of granular materials such as avalanching in sand piles and the formation of slip planes in materials under compression. Consequently, increasingly, simulation studies using techniques such as discrete element modelling (DEM) provide an invaluable method of investigating the particle-scale interactions underlying granular material response in a range of disciplines including chemical engineering [11; 3; 24], mechanical engineering [10], soil mechanics [23; 4; 15; 7], pharmaceuticals [13], agriculture and food processing.

DEM simulations model granular material at the particle scale. Based on classical mechanical ideas, equations detailing the forces acting on each individual particle are derived. These equations are integrated in time, and at each timestep the position, translational and rotational velocity, forces and torques acting on each individual particle are calculated. Since DEM simulations typically use thousands, even hundreds of thousands, of particles there are significant questions as to how best to extract physical understanding from the data. At the most basic level, it is often impractical to output all information at every timestep of the numerical integration, and a decision on how frequently to output data has to be made. As a result, data from simulations is typically presented in one of two ways. Either individual particle information is used to calculate bulk properties such as coordination number and porosity as in [17; 24] or snapshots of the sample at a few selected times are given showing individual particles/regions coloured according to their velocity, cumulative rotation, displacement or the magnitude of the contact forces between neighbouring particles, see for example, [7].

Post-processing of DEM data using wavelet techniques has been found to be effective in investigating hopper flows. [18; 19; 22]. In this paper, we explore the use of wavelet techniques to analyse data from a different physical scenario: a relatively dense sample under planar biaxial strain. This exhibits a strain-softening type phenomena and a distinct localization post-peak is evident [16]. As a consequence of the localizations, the post-peak response is not homogeneous throughout the specimen and these simulations are well-suited to assess whether the wavelet analysis method can effectively capture inhomogeneities in granular material response.

We focus on the three quantities: the relative variation of the major and minor principal stresses, the porosity and the coordination number. By splitting the sample into a number of sub-regions we illustrate how wavelets enable typical scales on which “peak events” in axial stress, porosity and coordination number occur to be identified. Furthermore, the location of the regions both in strain (time) and space where “peak events” occur can be found. We show that the strain/space regions of “peak events” compare well with regions of maximum cumulative rotation of the particles. We also use cross-correlation to show that changes in porosity are correlated to changes in axial stress on some wavelet scales.

Although the results we present are for an analysis of a DEM simulation in two space dimensions, the wavelet method can be readily extended to analysis of data from three-dimensional simulations. Since the wavelet analysis does not require large quantities of data, the method could be used as a pre-processing tool to identify an appropriate sampling strain and a strain/space region for more data intensive methods to focus on.

The paper is organised as follows. In section 2 details of the DEM biaxial compression simulations are given and in section 3 we give a brief outline of the wavelet transform. The results of the application of wavelet analysis to local averages for stress, porosity and coordination number are presented in section 4 along with a comparison with plots of the cumulative particle rotations from the same simulation studies. We end with a brief summary of the main findings to date in section 5.

2 Simulation details

Data from simulations of biaxial compression tests on dense two dimensional assemblies of disks, as given in [16], was considered. The simulations were from two different specimens with different numbers of particles. Specimen A consisted of 5728 disks in a region initially of width 9 cm and height 18 cm. Specimen B consisted of 12512 disks in a region initially of width 18cm and height 36cm. The particle radii were uniformly distributed between 0.075 cm and 0.100 cm with an initial porosity in both cases of 0.01. The specimens were bounded above and below by rigid walls, while the lateral boundaries were modelled using a "stress controlled membrane" that mimics the latex membranes typically used in soil mechanics triaxial tests. This works by identifying the exterior discs and forces are applied to these discs so that the stress applied along the two vertical boundaries remains constant during the simulation. The specimens were compressed in a strain controlled simulation, with the top boundary moving downwards at a constant velocity of 0.02981 cm/s for specimen A and 0.02966 cm/s for specimen B. The simulations were carried out using the PFC 2D code (Itasca [9]). In both the normal and shear directions the contact was modelled using linear springs with a stiffness of 5×10^7 N/m, the density of the disks was assumed to be $2 \times 10^9 \mathrm{kg/m}^3$ (scaled to reduce simulation time), the global damping coefficient was set to 0.2, and the coefficient of interparticle friction was assumed to be 0.3, typical of smooth dry near-spherical particles [21]. Further details of the simulation approach can be found in [14]. We note that density scaling is often used in quasi-static simulations and does not alter the underlying observed physical phenomena. For example, Thornton [23] scaled his particle densities by a factor of 10^{12}. O'Sullivan *et al.* [16] scaled their density values by a factor of 10^4 for their two dimensional simulations and these simulations were carefully validated against physical test data. Care was taken to ensure that the particles were in a "quasi-static" state throughout the simulations presented here (the forces along the top and bottom boundaries were monitored to ensure that they were approximately equal). The simulations for specimen A/B were run to total axial strains of 12% and 15.5% respectively.

As noted above, the simulations have the capacity to produce large amounts of data. Two different sets of data for each simulation were recorded. In the first set, the total axial strain was divided into 25 intervals. For each strain interval the total cumulative rotation for each particle in the interval was calculated and saved. The second set of data consisted of measurements of the porosity, coordination number and principal stress ratio averaged over specified sub domains. In order to retain some spatial information, 23 circular sub-domains or "measurement circles" were selected, as illustrated for specimen A in Figure 1. A circular geometry for the

sub-domains was used as it is an inbuilt function within PFC. Information was output at axial strain intervals of 8.1152×10^{-6} for specimen A and axial strain intervals of 5.4374×10^{-6} for specimen B.

The coordination number, N was calculated using

$$N = \frac{2N_c}{N_p}, \tag{1}$$

where N_c is the number of contacts within the measurement circle and N_p is the number of particles. The average stress tensor $\bar{\sigma}_{ij}$ was calculated from

$$\bar{\sigma}_{ij} = \frac{1}{V}\Sigma_{c=1}^{N_c} l_i^c f_j^c \quad (i,j = x,y) \tag{2}$$

where V is the area of the measurement circle, f_j^c is the contact force vector at contact c, $l_i^c = x_i^b - x_i^a$ is the branch vector connecting two contacting particles, a and b, with centroids x_i^a and x_i^b. From the stress tensor the principal stress ratio

$$\frac{\sigma_1 - \sigma_3}{\sigma_1 + \sigma_3},$$

was constructed, where σ_1 and σ_3 are the principal stresses calculated from the eigenvalues of the stress tensor. The data was saved at equal strain intervals and the position of the measurement circles remained fixed during loading.

The biaxial simulations considered in this study are analogous to strain controlled triaxial tests typically used in experimental soil mechanics to analyse soil response characteristics. In a physical test the specimen is subject to an all round confining pressure, σ_r and the deviator stress, $\sigma_a - \sigma_r$, is measured using a load cell placed between the specimen and the loading frame. Since the stress ratio, $\frac{\sigma_a - \sigma_r}{\sigma_a + \sigma_r}$, versus strain is a common way of representing laboratory data, the analogous quantity was also computed from the simulation. In the simulation, σ_r is equivalent to the stress imposed along the vertical boundaries, and the axial stress σ_a is determined by integrating the contact forces along the rigid horizontal boundaries.

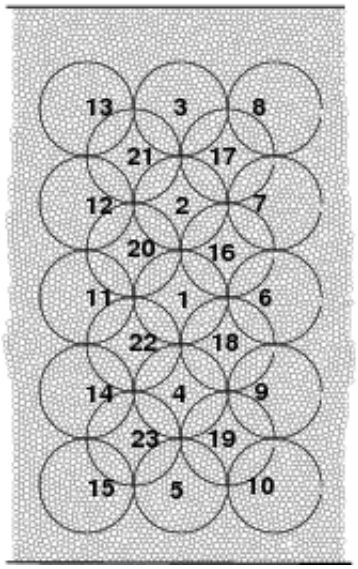

Fig. 1 The position of the 23 different measurement circles on Specimen A

3 Wavelet analysis

The wavelet transform is a method of converting a signal or function into another form which either makes features of the original signal more amenable or allows the original data set to be described more succinctly. The better known fast Fourier transform allows one to split a signal up according to the amount (weight) of the signal at each frequency. The wavelet transform is similar, but instead of using global basis functions like sine and cosine, considers basis functions that are localized in space. Consequently, wavelet transform techniques, unlike Fourier transforms, are particularly good for studying signals/time series that are non-stationary and/or contain sudden jumps. The basis functions, $\psi_{j,k}$, used by the wavelet analysis are derived from a "mother wavelet" $\psi(t)$ and are defined by a series of j dilations and k translations,

$$\psi_{j,k}(t) = \frac{1}{\sqrt{a_0^j}}\,\psi\left(\frac{t - kb_0a_0^j}{a_0^j}\right), \tag{3}$$

where $a_0 > 1$ is fixed and gives the dilation factor and $b = b_0a_0^j$ is the translation step at scale j. Here, we choose $a_0 = 2, b_0 = 1$ so that both dilation and translation are based on powers of two. This is known as dyadic sampling.

The particular kind of wavelet analysis considered is known as a multiresolution analysis (MRA). This takes a signal/time series of the form $x(t_n), n = 1..N$ and splits it into two sets of subsignals. The first set of subsignals is known as the details D_j, and are defined by

$$D_j = \sum_{k=1}^{N} d_{i,j}\,\psi_{j,k} \tag{4}$$

where the weights, $d_{i,j}$ are given by

$$d_{i,j} = \sum_{n=1}^{N} x(t_n)\psi_{j,k}(t_n). \tag{5}$$

The details give the amount of the signal at each wavelet scale, where D_1 is the finest scale. The second set of subsignals is known as the approximations and is defined by

$$A_j = x - \sum_{i=1}^{j-1} D_i \tag{6}$$

Each approximation A_j represents the signal with all the finer structure (detail) contained in the $j-1$ details filtered out.

There are several different mother wavelets that are commonly used, each has a different shape and is localized over a different numbers of data points, that is, has different "support". Which wavelet is appropriate for a given time series depends on the features that one wishes to extract: if a feature has a particular shape then a wavelet that mimics that shape will reflect most clearly the characteristics of this feature. For example, if the signal contains sudden jumps between different levels, then a wavelet that has jumps, such as the Haar wavelet, will show best how big and where the jumps occur. In DEM simulations of granular processes the time series tend to be spiky and it is for this reason that the Daubechies wavelet db2 was used. Fuller discussion of the issues relating to wavelet choice are given in [8; 6; 2].

A thorough guide to the theory underlying wavelets is given in [20]. For a survey of the application of wavelets to different physical problems see in [2] and for a practical guide to the implementation of wavelet analysis see [5]. The MRA contained in this paper was performed using MATLAB.

4 Results

4.1 Specimen A

We first consider the simulation results for the axial stress $\frac{\sigma_a - \sigma_r}{\sigma_a + \sigma_r}$ as a function of axial strain. As can be seen in Figure 2, the response of the specimen is analogous to the response of a slightly dense sand, the stress ratio increases up to a peak value of 0.376 at an axial strain of 1.2%. Post-peak, there is a decrease in the mobilised stresses, with a residual stress ratio of about 0.25 being attained between 6% and 12% strain.

In Figure 3 the results of applying an MRA to the stress ratio are presented. In Figure 3 (a) the stress ratio versus strain is shown whereas each of the detail coefficients, D_2 through to D_8 are shown in Figures 3 (b)-(h) respectively. The maximum of the stress ratio can be identified particularly well in D_2, D_3 and D_4 where there is a sharp transition from a wavelet coefficient that is very small to one that is moderate at a strain value of 1.2%.

In order to investigate whether any spatial structure was visible using the MRA technique, MRA was applied to the principal stress ratio data for each measurement circle. A typical set of results is shown in Figure 4, in this case for circle 21. The graph in Figure 4(a) shows the principal stress ratio versus the axial strain for circle 21. This data shows similar characteristics to the stress ratio from the bulk response (as illustrated in Figure 2) with a relatively smooth increase to a local maximum value of 0.3435 at an axial strain value of 1.17% before levelling off to an approximately constant level.

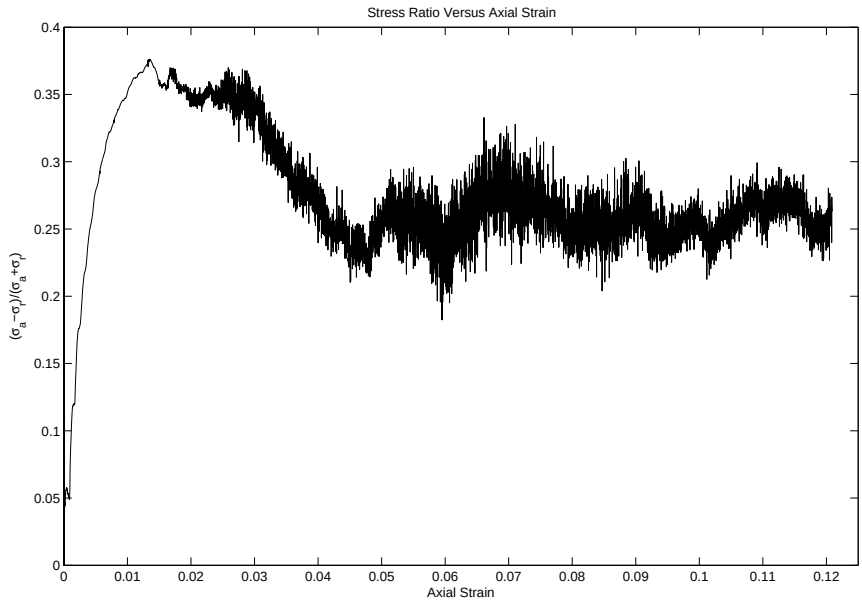

Fig. 2 Specimen A: Stress ratio $\frac{\sigma_a-\sigma_r}{\sigma_a+\sigma_r}$ versus axial strain.

Detail	strain scale (%)	space scale (cm)	space scale (mean particle diameters)
D1	0.0008	0.000146	0.0017
D2	0.0016	0.000292	0.0033
D3	0.0032	0.000584	0.0067
D4	0.0065	0.001168	0.0134
D5	0.0130	0.002337	0.0267
D6	0.0260	0.004674	0.0534
D7	0.0519	0.009349	0.1684

Table 1 Strain and space scales related to the detail coefficients for specimen A. The space scale in mean particle diameters is calculated by dividing the space scale measured in centimetres by the mean particle diameter, 0.0875cm.

Figure 4(b)-(h) show the wavelet detail coefficients D_2 through to D_8. Note that the maximum value of the magnitude of the coefficients for the lower detail coefficients is small suggesting that principal stress ratio changes on scale of D_2, D_3 and D_4 are small. As is particularly clear in D_7, there are a number of peaks events that are localized in strain. Each detail corresponds to a different strain scale. Using the strain and the height of the specimen one can also relate the strain to a space scale, as summarised in Table 1.

Similar peaks were seen in the wavelet analysis for the other 22 circles. In order to systematically identify if the peaks in the details correlated to a particular spatial structure/time structure, for each circle, each detail D_j, was divided into 25 equal intervals in time. For each interval, the maximum absolute value of the detail coefficient was evaluated. Each circle was then shaded according to this value. Typical examples are shown in Figure 5 for D_3, D_7 and D_8 and for three different axial strain intervals.

In D_3 (and similarly for D_2, not shown here), the sample appears fairly homogeneous with little variation in the shading in the main part of the specimen but significant activity in the corners. For the strain interval of

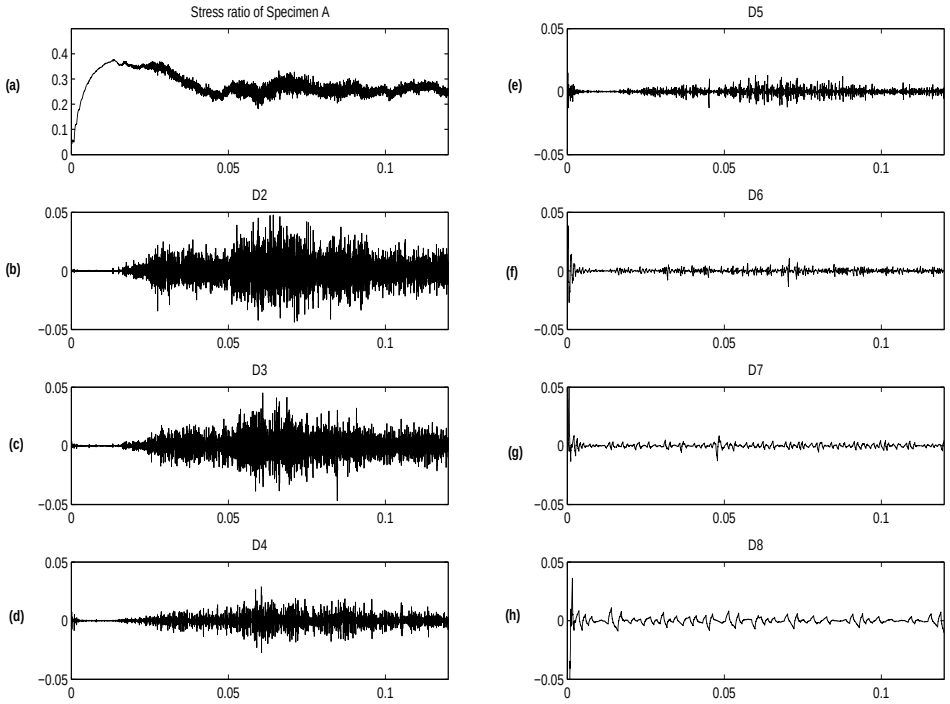

Fig. 3 Specimen A: MRA of the stress ratio $\frac{\sigma_a-\sigma_r}{\sigma_a+\sigma_r}$. (a) shows the stress ratio versus the strain, (b)-(h) show the detail coefficients D_2 through to D_8.

5.31% to 5.80% at scale D_7, Figure 5(d), the shading indicates that there is little spatial structure. However in the second strain interval, Figure 5(e), the maximum value of the detail coefficient D_7 is relatively large along a line from the top left sloping down to the middle at the the right. In the third strain interval, Figure 5(f), the sample is again much more homogeneous. At scale D_8 a similar pattern emerges, Figure 5(g)(i).

An MRA analysis of local porosity and coordination number was also carried out. Results are shown in Figures 6 for the detail D_7. Here it is particularly clear that maximum values of the detail coefficient D_7 occur along a line from the top left to bottom right and also that the magnitude of the maximum value as a function of strain: for example, in the first strain increment (5.31% to 5.80%) shown in Figure 6(a) and (d) the specimen appears much more homogeneous than in the second strain increment (5.80%-6.28%) (Figure 6 (c) and (d)).

These results may be compared with the cumulative rotation as shown in Figure 7 for the same strain intervals. The cumulative rotation is the net rotation experienced by each particle over the current strain interval. The cumulative rotations indicate that there is a clear localization of rotational activity, indicative of

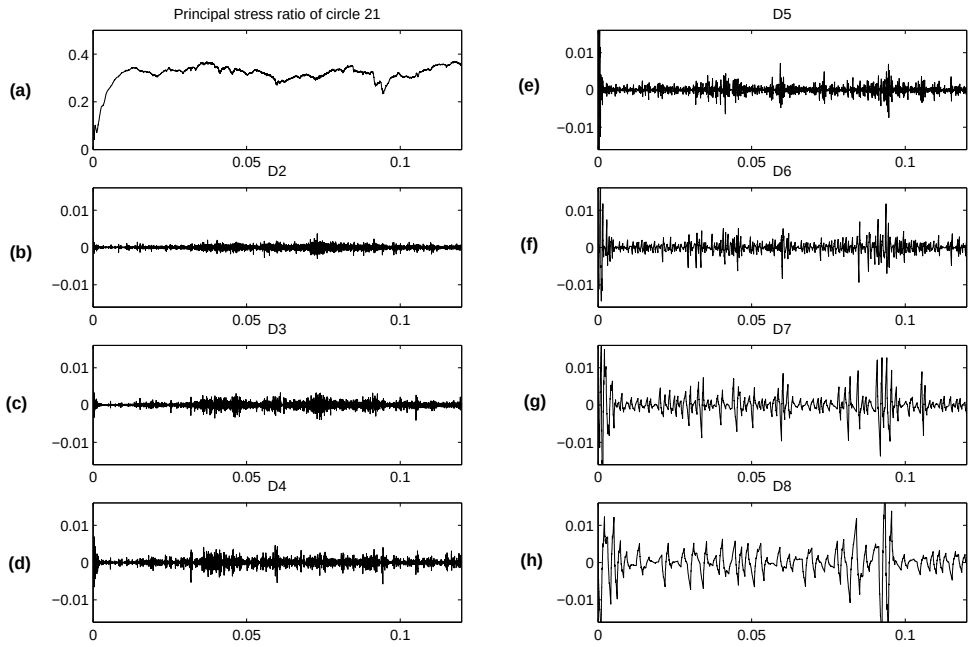

Fig. 4 MRA of the principal stress ratio $\frac{\sigma_1-\sigma_3}{\sigma_1+\sigma_3}$ for circle 21. (a) shows the principal stress ratio versus the strain, (b)-(h) show the detail coefficients D_2 through to D_8.

a shear band, along a line that passes through circles 13, 21, 2, 16 and 6 (see Figure 1) in a position consistent with the results from the MRA technique.

From Figure 7 it is also clear that the cumulative rotation is large in the corners of the specimen. This is a result of the lateral boundary conditions: the flexible membrane condition used in the simulation allows the particles to move more freely than if rigid boundary conditions were applied. While this means that localisations are seen more readily it also results in less lateral constraint and the consequent large cumulative rotation of the particles in the corners. This corner effect can also be seen in the wavelet coefficients D_3 (see Figure 5(1)-(c)).

4.2 Specimen B

In order to further test the wavelet technique, data from the second larger specimen was considered. This larger specimen shows a similar kind of response to specimen A: in Figure 8 the stress ratio versus the strain is shown for specimen B overlaid on the analogous graph for specimen A. The characteristic contact loading followed by slippage is again visible.

As for specimen A, specimen B was divided into 23 circles. Since the aspect ratio is the same as for specimen A, these have the same relative position as in specimen A but each circle contains more particles. The data for principal stress ratio, coordination number and porosity was analysed in an identical manner to that for specimen A: the MRA was applied and then the total strain interval was divided into 25 equal

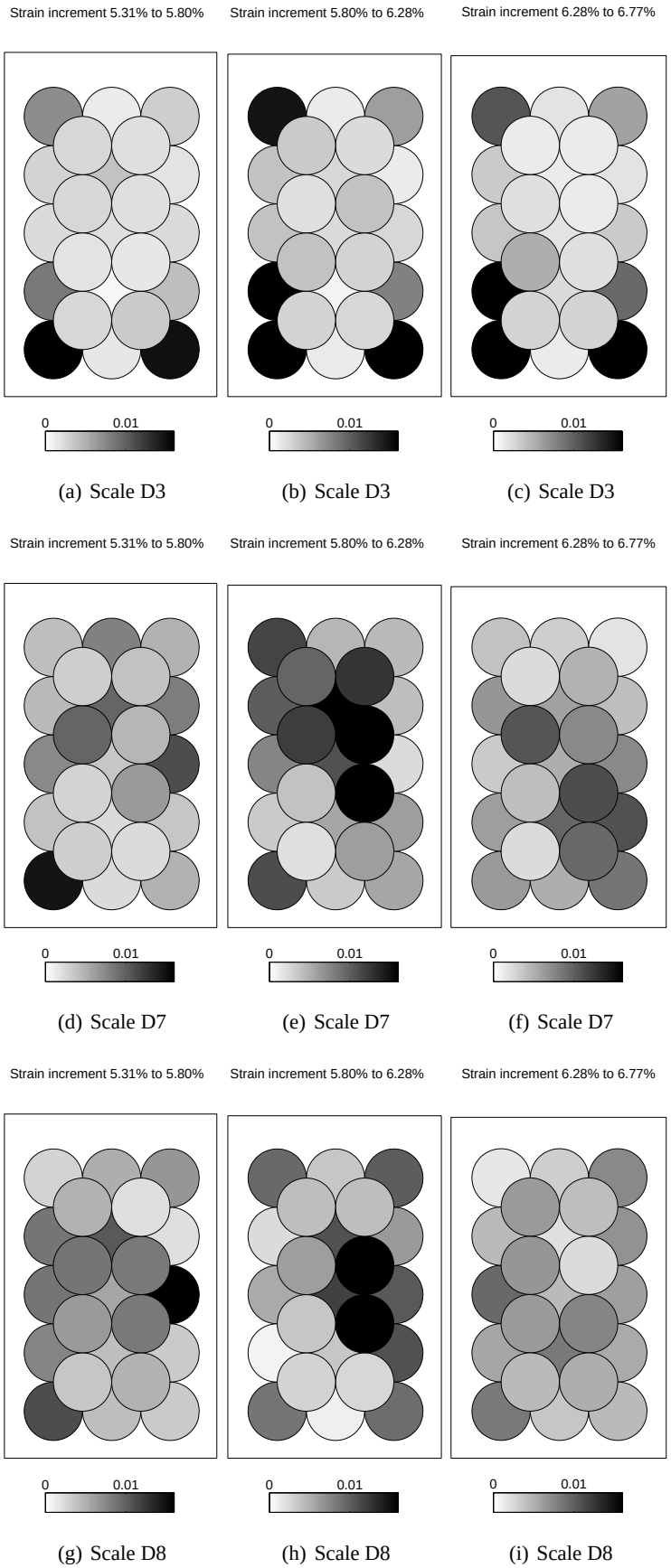

Fig. 5 Sub-regions of the sample shaded according to the magnitude of the MRA detail coefficients for the principal stress ratio (specimen A). Three different levels of detail (D_3, D_7 and D_8) and three successive strain increments (5.31%-5.80%, 5.80%-6.28% and 6.28%-6.77%) are shown.

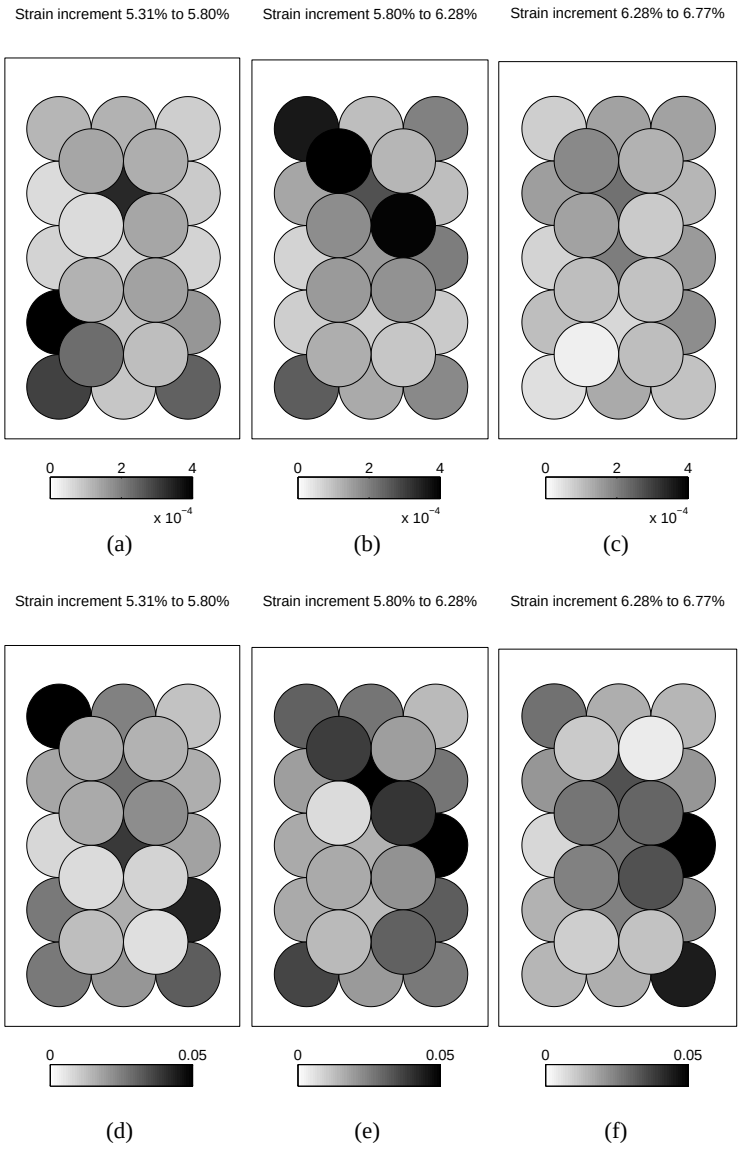

Fig. 6 Sub-regions of the sample shaded according to the magnitude of the MRA detail coefficients for (a-c) porosity and (d-f) coordination number at D_7. The same three strain intervals as shown for the principal stress ratio in Figure 5 (Specimen A) were used.

intervals and the circles were shaded according to the maximum absolute value of the MRA detail coefficient for each interval. Since again most activity was at the larger details, only D_7 is shown. The relation between the different detail coefficients and strain/space scales is given in Table 2. Figure 9 shows shaded circles for D_7 for stress ratio, porosity and coordination number for three strain intervals. The shading shows that D_7 is not homogeneous in either strain or space, with this time most activity typically occurring (for these strain intervals) along a line from the top right down to the middle left. These results can be compared to the localizations shown by the cumulative rotations in Figure 10.

It can be seen that in this particular case the localization passes through a region where the measurement circles overlap. In order to see if moving the measurement circles significantly changes the results, the 23

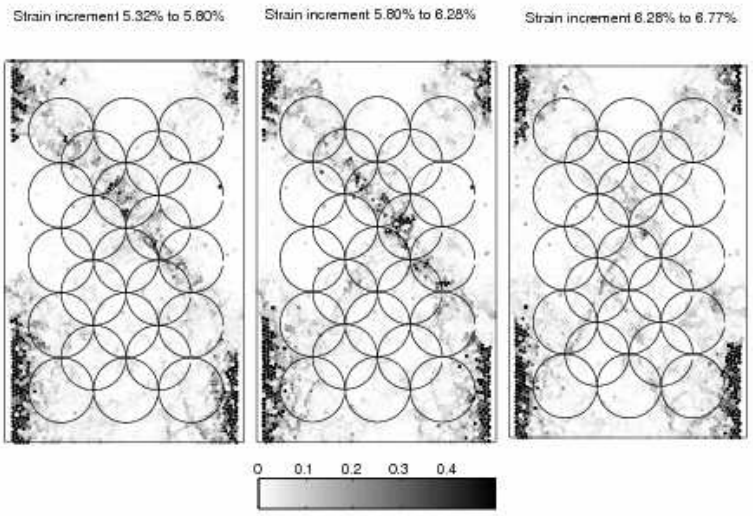

Fig. 7 Particles shaded according to the absolute value of their cumulative rotation for the three successive strain intervals used in Figures 5 and 6 (Specimen A). These cumulative rotation plots are useful for identifying visually the location of slip planes in the specimen.

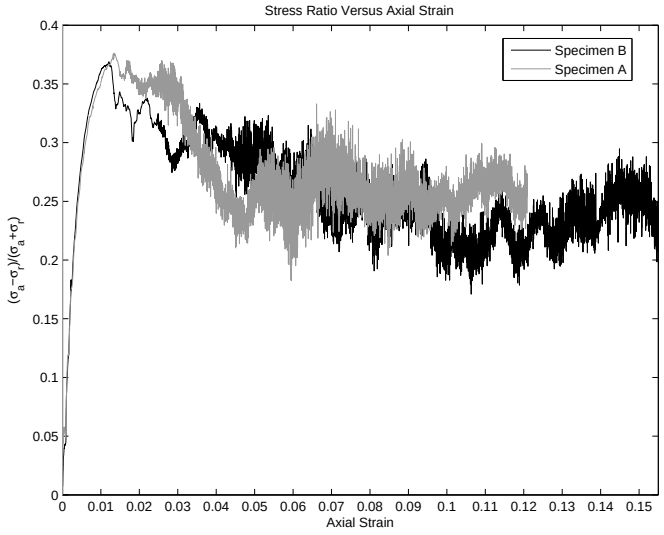

Fig. 8 Stress ratio $\frac{\sigma_a-\sigma_r}{\sigma_a+\sigma_r}$ versus axial strain for specimens A and B.

measurement circles for specimen B were moved down and, as shown in Figure 11 and the MRA calculations repeated. Figure 12 shows shaded circles corresponding to their magnitude of MRA in each axial strain, where only D_7 has been shown. The localization is still visible, although the shading within individual circles is, not surprisingly, different.

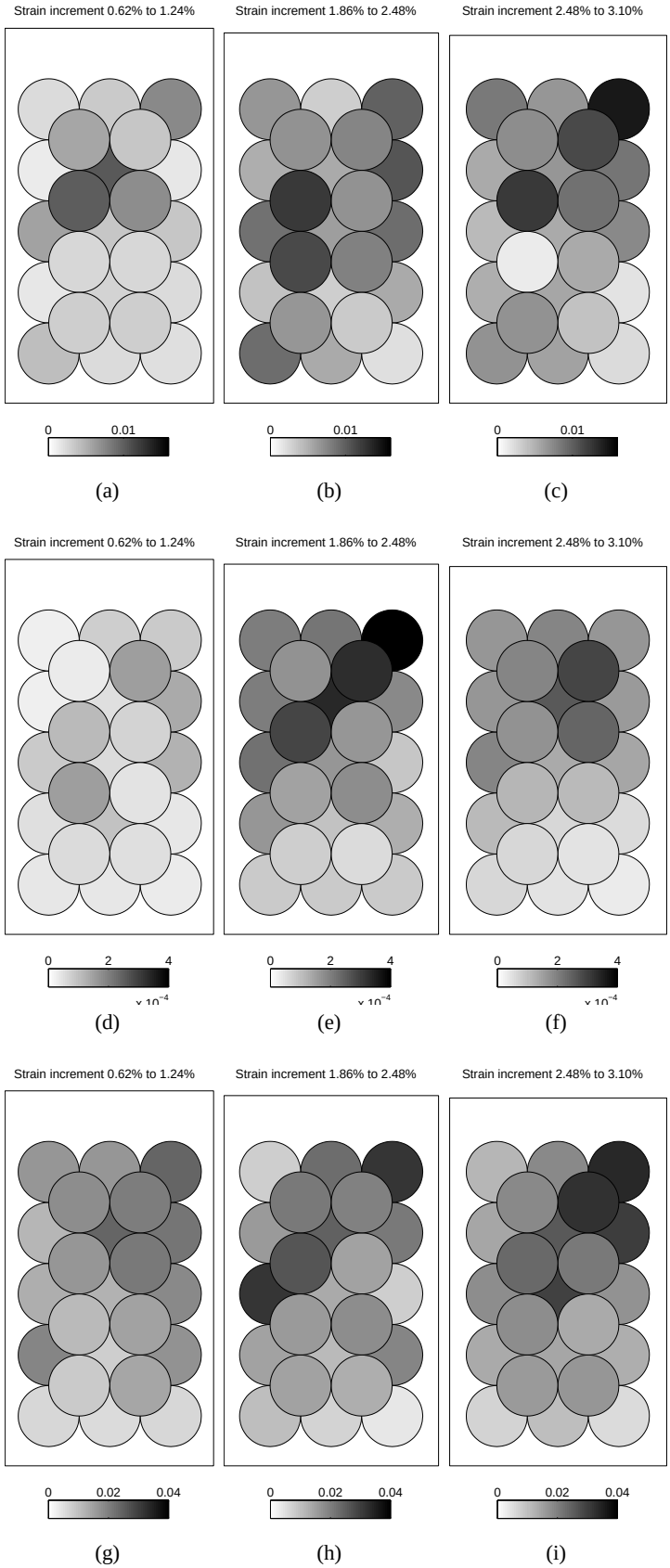

Fig. 9 Sub-regions of the sample shaded according to the magnitude of the MRA detail coefficient D_7 for specimen B. Three different strain intervals, 0.62%-1.24%, 1.86%-2.48% and 2.48%-3.10%, are shown. (a-c) stress; (d-f) porosity; (g-i) and coordination number.

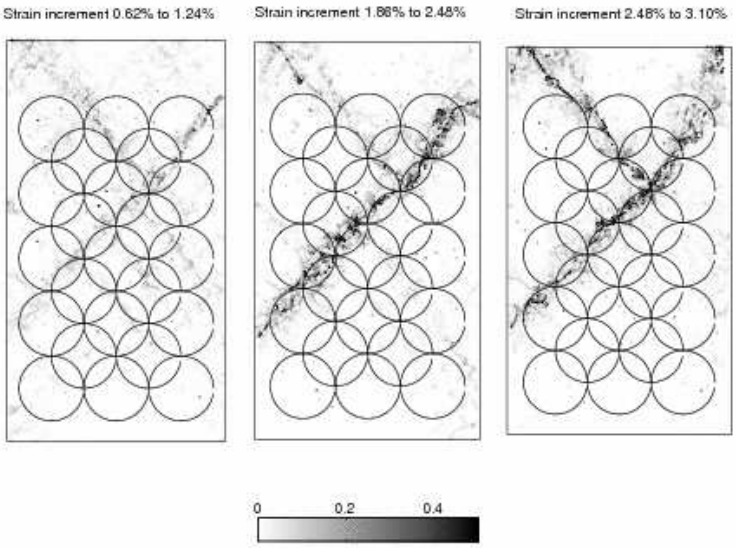

Fig. 10 Particles shaded according to the absolute value of their cumulative rotation for the three different axial strain intervals used in Figure 9 (Specimen B). The position of the sub-regions are also shown.

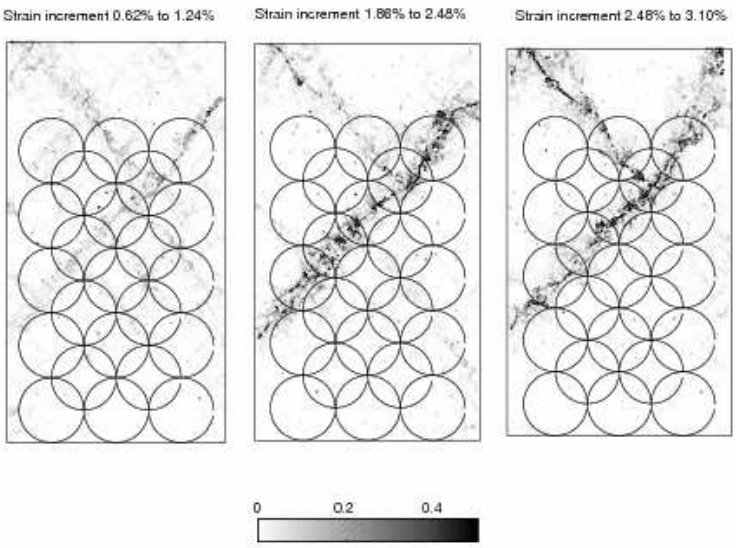

Fig. 11 New position of the sub-regions once the measurement circles have been moved down. The cumulative rotations for the same strain intervals as those shown in Figure 10 are also plotted.

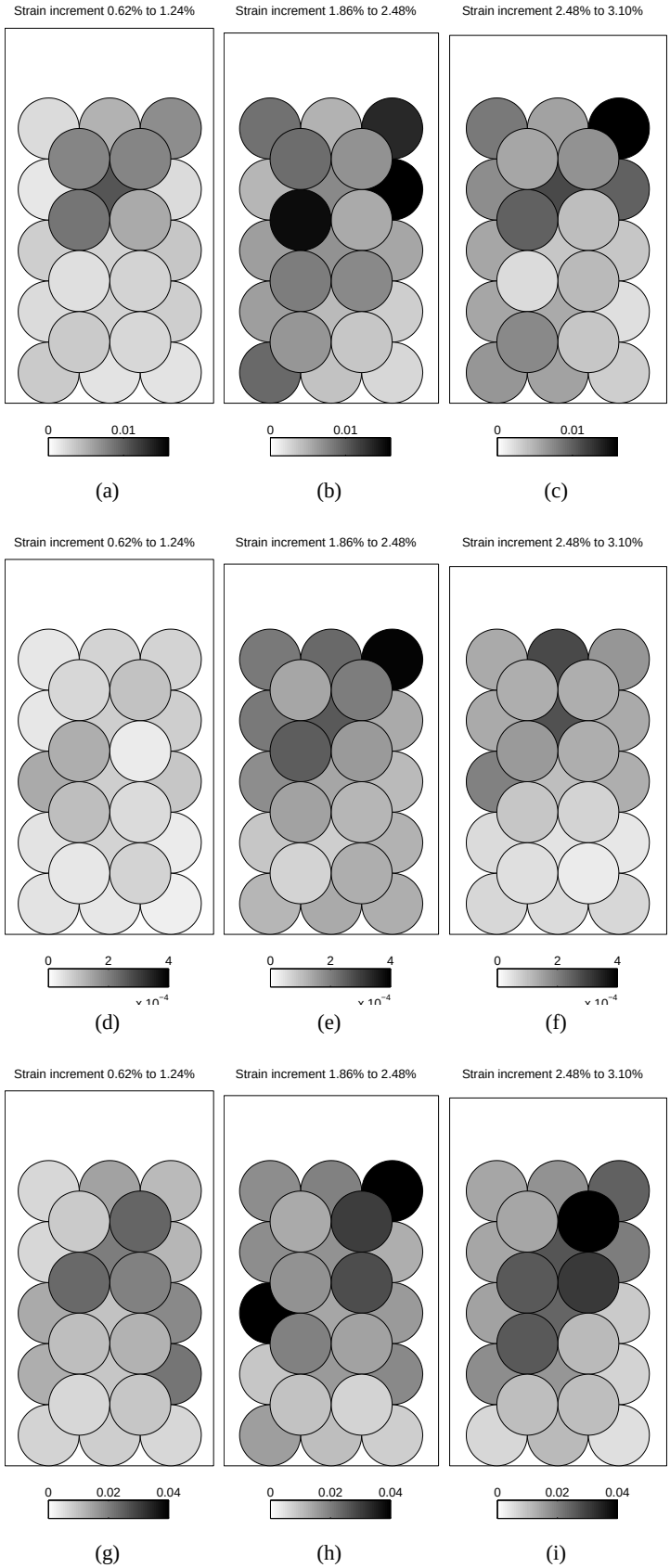

Fig. 12 Sub-regions shaded according to the maximum absolute value of the MRA detail coefficient D_7 for (a-c) stress; (d-f) porosity; (e-h) coordination number (Specimen B). The same three strain intervals used for Figure 9 are shown

Detail	strain scale (%)	space scale (cm)	space scale (mean particle diameters)
D1	0.0005	0.000196	0.0022
D2	0.0011	0.000391	0.0045
D3	0.0022	0.000783	0.0089
D4	0.0043	0.001566	0.0179
D5	0.0087	0.003132	0.0358
D6	0.0171	0.006264	0.0716
D7	0.0348	0.012528	0.1432

Table 2 Space and strain scales related to detail coefficients for specimen B. The space scale in mean particle diameters is calculated by dividing the space scale in centimetres by the mean particle diameter, 0.0875cm.

5 Cross Correlations

The wavelet transform picks up local fluctuations in stress ratio, porosity and coordination number at different scales of strain. In order for a slip plane to form in densely packed materials it is believed that not only should there be a local increase in the stress but local dilation of the specimen must occur: in the extreme case of hexagonally packed identical circular disks, the disks cannot roll relative to each other without sliding to a face-centred cubic configuration first. Since hexagonal packed circles have a packing fraction of 0.907 and face-centred cubic packed circles have a packing fraction of 0.785 this means that a local dilation of 13% must occur [1; 12]. Along a slip plane, one might therefore expect to see a correlation between peak events in the stress ratio and significant changes in the porosity. There is some evidence that this might be the case in Figure 5 and Figure 6 for specimen A and in Figure 9 for specimen B. In order to investigate further if such a correlation exists, the cross-correlation of the wavelet coefficients for the porosity and the stress ratio was carried out. Specifically, for each circle i, the detail coefficient D_j consists of a series of k values. If $S_{ij}(k)$ represents the detail coefficients for the stress ratio for circle i and detail level j and $P_{ij}(k)$ represents the detail coefficient for the porosity for circle i and detail level j then the cross-correlation r_0 is defined by

$$r_0 = \frac{\sum_k (S_{ij}(k) - \bar{S_{ij}})(P_{ij}(k) - \bar{P_{ij}})}{\sqrt{\left(\sum_k S_{ij}(k)^2 - n\bar{S_{ij}}^2\right)\left(\sum P_{ij}(k)^2 - n\bar{P_{ij}}^2\right)}}, \tag{7}$$

where $\bar{S_{ij}}$ is the mean value of $S_{ij}(k)$ and $\bar{P_{ij}}$ is the mean value of $P_{ij}(k)$.

It might also be that a change in porosity occurs as a result of, but at a later time, than a change to the stress ratio. This can be investigated by considering the cross-correlation of one series lagged with respect to the other, specifically for lag d one calculates

$$r_d = \frac{\sum_k (S_{ij}(k) - \bar{S_{ij}})(P_{ij}(k+d) - \bar{P_{ij}})}{\sqrt{\left(\sum_k S_{ij}(k)^2 - n\bar{S_{ij}}^2\right)\left(\sum P_{ij}(k+d)^2 - n\bar{P_{ij}}^2\right)}}, \tag{8}$$

Cross-correlation calculations between the absolute values of the detail coefficients for the stress ratio and porosity for each circle and for all reasonable lags were carried out. Each circle was then shaded according to the magnitude of the cross-correlation coefficient, as shown for D_5 for specimen A in Figure 13. This Figure shows that there is moderate cross-correlation between the stress ratio and the porosity along a diagonal line through circles 13,21,2 and 16, the same line along which the incremental rotation is largest. The values of the

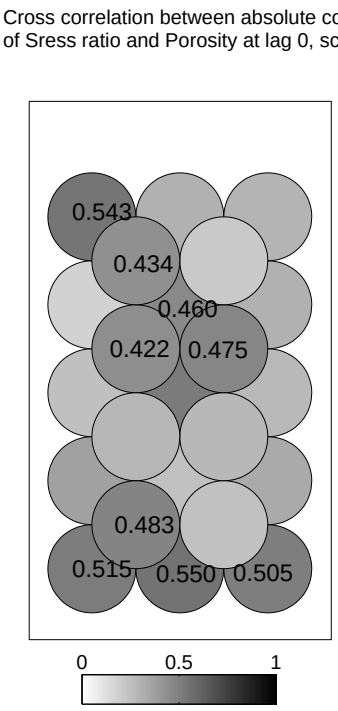

Fig. 13 Sub-regions shaded according to the absolute value of the cross correlation of stress ratio with porosity for D_5 for each circle. There is no lag.

cross-correlation coefficients were investigated to confirm whether or not they were statistically significant. In order to do this, a student t-test was applied to the hypothesis that there was no cross-correlation. In order to apply this test we consider the value of

$$t = \frac{r(d)\sqrt{n-2}}{\sqrt{1-r(d)^2}},$$

where n is the number of data points in the time series. For specimen A and detail D_7 the $n = 117$. If, for example, $r(d) = 0.422$, then this gives a value of $t = 4.99$ and we can reject the hypothesis that there is no cross-correlation with a certainly of more than 99%. Consequently even though the values of the cross-correlation along the slip plane are not greater than 0.5, the cross-correlation is still significant.

Interestingly, only small values of the cross-correlation coefficients were found for the lagged details, indicating that changes of stress ratio and porosity occur effectively simultaneously. Cross-correlation calculations for specimen B were inconclusive: for specimen B the circles have a diameter of approximately 60 particle diameters (as compared with 30 particle diameters for specimen A). Consequently, it may be that although peak events in a circle are identifiable, some of the detail required for cross-correlation is averaged out.

6 Conclusion

We have shown how an MRA analysis of data from a DEM simulation of two different specimens subject to a planar biaxial strain can aid in finding the time/strain scales on which significant events occur. This information could be used to determine how frequently to output data. For example, for Specimen A, key scales for cross-correlation and for peak events were on the detail scale of D_5 and above, suggesting that data could have been reduced by a factor of 32 without losing significant information. Furthermore, by dividing the specimen down into regions in space and considering intervals in strain we were able to find both when and where peak events occur. These matched well with results from a study of the incremental rotation. Using cross-correlation we were able to show that the geometric property of porosity correlates with the principal stress ratio along the slip plane for specimen A. The technique can readily be applied to data from simulations in three space dimensions as well as two space dimensions.

Acknowledgements N. Meejun thanks the Thai government for her scholarship as part of the Thai-UK Collaborative Research Network.

References

1. Abou-Chakra,H and U Tüzün (1999) Coefficient of friction of binary granular mixtures in contact with a smooth wall, part b: Micro-structureal model describing the effects of packing fraction and load distribution on the wall friction of smooth, elastic spheres. Chemical Engineering Science 54:5913–5925
2. Addison P (2002) The illustrated wavelet transform handbook. Institute of Physics, Bristol, UK
3. Baxter J, Abou-Chakra H, Tüzün U, Lamptey BM (2000) A dem simulation and experimental strategy for solving fine powder flow problems. Trans I Chem E 78A:1019–1025
4. Cheng Y, Nakata Y, Bolton M (2003) Discrete element simulation of crushable soil. Géotechnique 53:633–641
5. la Cour-Harbo A, Jensen A (2001) Ripples in mathematics. Spring-Verlag, Berlin and Heidelberg GmbH & Co K
6. CTorrence, Compo G (1998) A practical guide to wavelet analysis. Bulletin of the American Meteorological Society 79(1):61–78
7. Cui L, O'Sullivan C (2006) Exploring the macro- and micro-scale response of an idealised granular material in the direct shear apparatus. Géotechnique 56:455–468
8. Farye M (1992) Wavelet transforms and their applications to turbulence. Annu Rev Fluid Mech 24:395–457
9. Group IC (1998) PFC2D 2.00 particle flow code in two dimensions. Itasca Consulting Gropu, Inc,: Minneapolis, Minnesota
10. Iordanoff I, Charles J, Berthier Y (2007) Discrete element model: a helpful tool for abrasion process study. Proceedings of the Institution of Mechanical Engineers, Part B: Journal of Engineering Manufacture 221
11. Langston P, Tüzün U, Heyes D (1995) Discrete element simulation of granular flow in 2d and 3d hoppers: dependence of discharge rate and wall stress on particle interactions. Chemical Engineering Science 50:967–
12. M GR (1989) Particle packing characteristics. Princeton, N.J. : Metal Powder Industries Federation
13. Martin C, Bouvard D, Shima S (2003) Study of particle rearrangement during powder compaction by the discrete element method. J Mech Phys Solids 51:667–693
14. O'Sullivan C (2002) The application of discrete element modelling to finite deformation problems in geomechanics. PhD thesis, Department of Civil Engineering, University of California, Berkeley
15. O'Sullivan C, Bray J, Riemer M (2002) Influence of particle shape and surface friction variability on response of rod-shaped particulate media. Journal of Engineering Mechanics 128:1182–1192
16. O'Sullivan C, Bray J, Li S (2003) A new approach for calculating strain for particulate media. International Journal for numerical and analytical methods in geomechanics 27:859–877
17. Rothenberg L, Kruyt N (2004) Critical state and evolution of coordination number in simulated granular materials. International Journal of Solids and Structures 41:5763–5774
18. Smith L, Tüzün U (2002) Stress, voidage and velocity coupling in an avalanching granular heap. Chemical Engineering Science 57:3795
19. Smith L, Tüzün U (2004) Planar and axially symmetric slow shearing granular flows: a comparitive evaluation of assembly evolution incorporating wavelet transforms. Chemical Engineering Science 59:3223–3234
20. Strang G, Nguyen T (1997) Wavelets and Filter Banks. Wellesley-Cambridge Press
21. Tüzün U, Adams M, Briscoe B (1988) An interface dilation model for the prediction of wall friction in a particulate bed. Chemical Engineering Science 43:1083–1098
22. Tüzün U, Baxter J, Heyes D (2004) Analysis of the evolution of granular stress-strain and voidage states based on dem simulations. Philosophical Transactions of the Royal Society London A 362:1931–1951
23. Thornton C (2000) Numerical simulation of deviatoric shear deformation in granulat media. Géotechnique 50:43–53

24. Yang R, Zou R, Yu A (2000) Computer simulation of the packing of fine particles. Physical Review E 62:3900–3908